Journal of Cluster Science (2025) 36:177
https://doi.org/10.1007/s10876-025-02897-w

ORIGINAL PAPER

Observation of Boron Bonds in Aromatic Boron Water Complexes $B_{13}(H_2O)_n^+$ (n = 1,2) and $B_{12}H(H_2O)^+$ Analogous to Benzene

Ting Zhang[1,2] · Rui-Nan Yuan[1] · Qiang Chen[1] · Si-Dian Li[1]

Received: 4 June 2025 / Accepted: 31 July 2025

Abstract

Gas-phase B_n^+ monocations exhibit strong hydrophilicity due to the prototypical electron-deficiency of boron. Joint chemisorption experiment and first-principles theory investigations performed herein indicate that the experimentally known planar magic-number C_{2v} B_{13}^+ can react with H_2O at room temperature to form a series of quasi-planar aromatic boron water complexes C_1 $B_{13}(H_2O)^+$ (**1**), C_2 $B_{13}(H_2O)_2^+$ (**2**), and C_1 $B_{12}H(H_2O)^+$ (**3**) analogous to benzene C_6H_6. Extensive theoretical calculations and analyses unveil their chemisorption pathways, bonding patterns, and more importantly, the effective in-phase LP(H_2O:)→LV(B) orbital overlaps between the more electronegative O atom in H_2O as lone-pair (LP) σ-donor and periphery electron-deficient B atoms in B_{13}^+ (B_3@B_{10}^+) and $B_{12}H^+$ (B_3@B_9H^+) with lone vacant (LV) orbitals as LP σ-acceptors, evidencing the existence of the newly proposed boron bonds in chemistry. A LP(H_2O:)→LV(B) boron bond in these boron water complexes possesses about 15 ~ 20% of the dissociation energy of a typical O–B covalent bond. Boron bonds are expected to exist in a wide range of boron-based complex systems with typical molecular ligands like H_2O, CO, and NH_3 as effective σ-donors.

Graphical Abstract

Joint chemisorption experiment and first-principles theory investigations indicate that B_{13}^+ monocation can react with H_2O to form a series of quasi-planar aromatic boron water complexes C_1 $B_{13}(H_2O)^+$, C_2 $B_{13}(H_2O)_2^+$, and C_1 $B_{12}H(H_2O)^+$ analogous to benzene, evidencing the existence of boron bonds in chemistry.

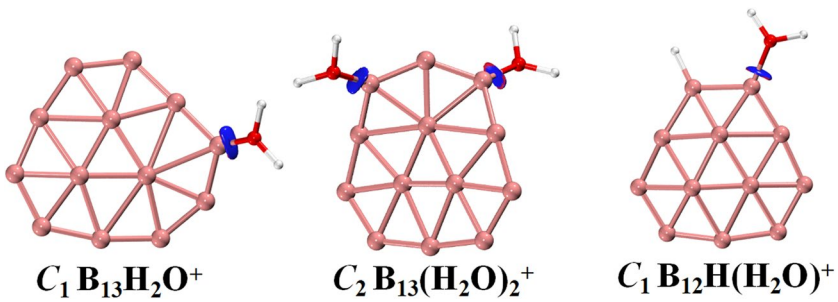

Keywords TOF-MS Spectroscopy · Boron Water Complexes · First-Principles Theory · Boron Bonds

Ting Zhang and Rui-Nan Yuan contributed equally to this work.

✉ Qiang Chen
chenqiang@sxu.edu.cn

✉ Si-Dian Li
lisidian@sxu.edu.cn

[1] Institute of Molecular Science, Shanxi University, Taiyuan 030006, China

[2] Department of Chemistry, Xinzhou Normal University, Xinzhou 034000, China

Introduction

As a prototypical electron-deficient element in the periodic table, boron ([He]$2s^2 2p^1$) exhibits unique structures and bonding in chemistry. Persistent joint photoelectron spectroscopy and first-principles theory investigations in the past two decades indicate that small boron clusters $B_m^{-/0}$ (m = 3-38, 41, 42) adopt planar or quasi-planar structures

Published online: 30 August 2025

[1–4], except the cage-like borospherenes D_{2d} $B_{40}^{-/0}$ and C_3/C_2 B_{39}^- [5, 6] and bilayer D_{2h} $B_{48}^{-/0}$ [7]. Combined ion mobility spectrometry and density functional theory studies reveal that B_m^+ monocations possess planar or quasi-planar structures for m = 12-15 and double-ring tubular geometries for m = 16-25 [8], with the magic-number B_{13}^+ ($B_3@B_{10}^+$) possessing a perfect planar C_{2v} configuration which, as a typical Wankel motor molecule with fluxional bonds (FBs), proves to be π-aromatic in nature analogous to benzene C_6H_6 [9–12].

Recent joint time-of-flight mass spectrometry (TOF-MS) and first-principles theory investigations by our group reveal that the planar or quasi-planar C_{2v} B_{13}^+, C_s B_{11}^+, and C_{2v} B_{15}^+ monocations can react with CO consecutively under ambient conditions to form a series of boron carbonyl aromatics (BCAs) $B_{13}(CO)_n^+$ (n = 1-7) analogous to benzene C_6H_6 [13] and $B_{11}(CO)_n^+$ (n = 1-6) and $B_{15}(CO)_n^+$ (n = 1-5) complexes with σ and π conflicting aromaticity analogous to benzene C_6H_6 and cyclooctatetraene C_8H_8 in π-bonding, respectively [14]. Although chemisorption reaction of B_{13}^+ with D_2O was firstly reported by Anderson's group using an ion trap instrumentation in 1990 [15] in which the dominant reaction channel observed involved the elimination of DBO to yield $B_{12}D^+$, detailed structures and bonding of the resultant boron water complexes still remain unknown to date. Previous theoretical calculations predict that the B_7 heptagons on metallo-borospherenes M&B_{40} can adsorb H_2O molecules and the quasi-planar B_{36} maintains its original quasi-planar configuration after H_2O adsorption [16, 17]. Our group predicted in 2025 the possibility of a series of the endohedral borafullerenes $X@B_{32}C_{36}$ (X = CH_4, BH_4^-, H_2O, and NH_3) analogous to the experimentally observed endohedral $H_2O@C_{60}$ [18] and proposed the concept of boron bonds (BBs) in chemistry which is defined as the in-phase LP(A:)-LV(B) orbital overlap between an electronegative atom A (A = O or N, here) as lone-pair (LP) σ-donor and an electron-deficient B atom with a lone vacant (LV) orbital as LP σ-acceptor [19]. However, direct experimental or joint experimental and theoretical investigations on LP(A:)-LV(B) boron bonds in boron-based complexes still remain elusive to date.

Joint TOF mass spectrum and first-principles theory investigations performed in this work indicate that the previously experimentally observed magic-number planar C_{2v} B_{13}^+ can react with H_2O at room temperature to form a series of aromatic boron water complexes C_1 $B_{13}(H_2O)^+$ (**1**), C_2 $B_{13}(H_2O)_2^+$ (**2**), and C_1 $B_{12}H(H_2O)^+$ (**3**) analogous to benzene, with $B_{13}(H_2O)^+$ as the primary product. These novel boron water complexes exhibit effective in-phase LP(H_2O:)→LV(B) orbital overlaps between the electronegative atom O in H_2O as LP σ-donor and periphery electron-deficient B atoms in B_{13}^+ ($B_3@B_{10}^+$) and $B_{12}H^+$ ($B_3@B_9H^+$) with LV orbitals as LP σ-acceptors, evidencing the existence of LP(H_2O:)-LV(B) boron bonds for the first time in boron water complexes.

Methods

Experimental Methods

A homemade reflection time-of-flight mass spectrometer (TOF-MS) equipped with a laser ablation ion source [20, 21], a quadrupole mass filter (QMF) [22], and a linear ion trap (LIT) reactor [23] was used in this work, as schematically illustrated in Fig. S1. Gas-phase boron cluster monocations (B_n^+) were prepared by laser ablation of a constantly translating and rotating pure ^{11}B isotope target (99% enriched), with 6 atm helium (He) introduced in as a carrier gas. Vaporization of the boron target was realized using a 532 nm pulsed laser (second harmonic of Nd^{3+}: yttrium aluminum garnet), with a single-pulse energy of 3-5 mJ and at a frequency of 10 Hz. Under these conditions, bare boron cluster monocations (B_n^+) were generated and size-selected by QMF. The size-selected magic-number B_{13}^+ clusters were filtered by QMF and led into the LIT reactor. Constrained within LIT, the B_{13}^+ monocations were cooled to room temperature by collision with a pulsed cooling gas of 2 Pa He for 2 ms and subsequently reacted with a pulsed injection of a reaction gas of 190 mPa He (99.99% enriched) which contains trace amounts of water impurities. B_{13}^+ reacted with H_2O impurities in the He reaction gas in LIT for the reaction time of t_r = 30 ms. Ultimately, the resultant product monocations were ejected from the LIT and mass-detected and analyzed by TOF-MS.

Theoretical Methods

Optimized structures of the observed boron water complexes $B_{13}(H_2O)^+$ (**1**), $B_{13}(H_2O)_2^+$(**2**), and $B_{12}H(H_2O)^+$ (**3**) are depicted in Fig. 2 at the hybrid PBE0 density functional theory level [24] with the 6-311+G(d,p) basis set combined with D3 van der Waals corrections implanted in Gaussian 16 program [25–27], with the corresponding intermediates (IMs) and transition states (TSs) collectively shown on the their chemisorption pathways in Fig. 3. Vibrational frequency checks were performed to make ensure that all IMs and TSs are the true minima and transition state of the systems, respectively. The relative energies were further refined by single-point calculations at the CCSD(T)/6-311+G(d,p) level [28–30], with the small diagnostic factors of T1 = 0.010-0.025. Born-Oppenheimer molecular dynamics (BOMD) simulation was performed on C_1 $B_{13}(H_2O)^+$ (**1**), C_2 $B_{13}(H_2O)_2^+$ (**2**) and C_1 $B_{12}H(H_2O)^+$ (**3**) at 300 K for

50 picoseconds using the CP2K program [31–33] to check the dynamic stability of the concerned complexes, with the GTH-PBE pseudopotential and the DZVP-MOLOPT-SR-GTH basis set used for boron, oxygen, and hydrogen. Intrinsic reaction coordinates (IRC) were calculated at PBE0-D3/6-311+G(d,p) to ensure that each transition state is linked to two appropriate intermediates [34, 35]. Detailed adaptive natural density partitioning (AdNDP) bonding pattern analyses were performed at PBE0/6-31G(d) on the concerned species [36]. Energy decomposition analyses with natural orbitals for chemical valence (EDA-NOCV) [37–39] were carried out utilizing the ADF 2022 package [40] at PBE0/TZ2P-ZORA level [41–43]. Non-covalent interactions reduced density gradient (NCI-RDG) analyses were performed to explore the bonding nature and identify the types of the non-covalent interactions using the Multiwfn program [44–46]. The bonding analysis, orbitals and RDG isosurfaces were visualized using the VMD software [47].

Results and discussion

Chemisorption Experiments

Previous gas-phase experiments indicated that B_{13}^+ is inert towards He, but reactive with H_2O [13]. Figure 1 shows the TOF mass spectrum of the size-selected B_{13}^+ reacting with trace amount of H_2O in the He reaction gas. The background TOF mass spectrum in Fig. 1(a) with a pulsed 2 Pa cooling He gas for 2 ms in the LIT shows a strong B_{13}^+ mass intensity at m/z = 143 and a weak $B_{13}(H_2O)^+$ peak at m/z = 161 due to the trace amounts of H_2O in the carrier gas. When the 190 mPa reaction gas was introduced into the LIT reactor with the reaction time of t_r = 30 ms after He cooling, four product signals are observed in the mass spectrum in Fig. 1(b): one effectively enhanced signal at m/z = 161 corresponding to $B_{13}(H_2O)^+$, two weak peaks at m/z = 133 and 151 corresponding to $B_{12}H^+$ and $B_{12}H(H_2O)^+$, respectively, and one weak but discernible signal at m/z = 179 evidencing the appearance of the bi-H_2O-chemisorption product $B_{13}(H_2O)_2^+$. The experimental results observed above indicate that B_{13}^+ can react with H_2O to produce $B_{13}(H_2O)^+$, $B_{13}(H_2O)_2^+$, $B_{12}H^+$ and $B_{12}H(H_2O)^+$ spontaneously in

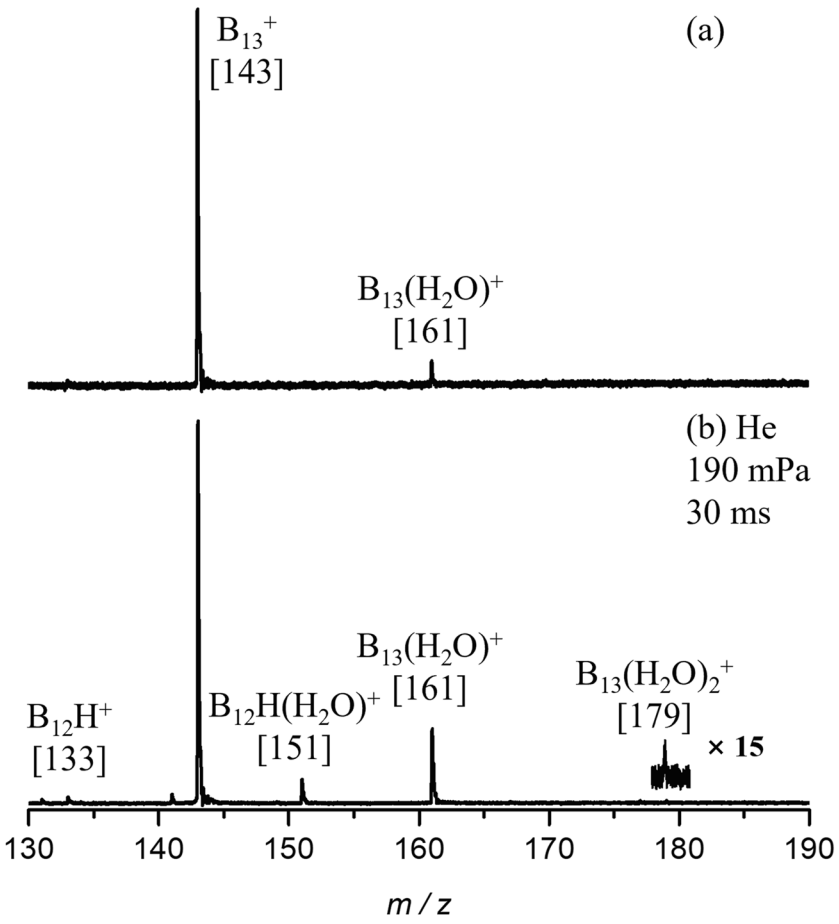

Fig. 1 (**a**) Background TOF mass spectrum of the mass-selected B_{13}^+ in He colling gas and (**b**) Measured TOF mass spectrum for the reactions of mass-selected B_{13}^+ with H_2O impurities in He reaction gas after He colling, with the mass signal of $B_{13}(H_2O)_2^+$ enlarged by 15 times. The cooling time is 2 ms and reaction time is 30 ms, with the reaction gas (He) pressure of 190 mPa

the following four reactions under ambient conditions, respectively,

$$B_{13}^{+} + H_2O \rightarrow B_{13}(H_2O)^{+} \quad (1) \quad \Delta E = -1.34 \text{ eV}$$
$$B_{13}(H_2O)^{+} + H_2O \rightarrow B_{13}(H_2O)_2^{+} \quad (2) \quad \Delta E = -1.29 \text{ eV}$$
$$B_{13}^{+} + H_2O \rightarrow B_{12}H^{+} + HBO \quad (3) \quad \Delta E = -1.33 \text{ eV}$$
$$B_{12}H^{+} + H_2O \rightarrow B_{12}H(H_2O)^{+} \quad (4) \quad \Delta E = -1.69 \text{ eV}$$

The negative calculated exothermicities of ΔE= −1.34, −1.29, −1.33, and −1.69 eV for reactions (**1**), (**2**), (**3**), and (**4**) at CCSD(T) level, respectively, indicate that the four observed products are all favorable in thermodynamics. Further analyses show that the H_2O-chemisorption reaction (**1**) and H_2O-activation reaction (**3**) have the comparable exothermicities of ΔE= −1.34 and −1.33 eV, respectively, consistent with the coexistence of both $B_{13}(H_2O)^+$ and $B_{12}H^+$ signals in the mass spectrum of the system in Fig. 1(b), with the former being partially converted to $B_{13}(H_2O)_2^+$ by chemisorption of the second H_2O through reaction (**2**) with the exothermicity of ΔE = −1.29 eV, while the latter being mostly converted to $B_{12}H(H_2O)^+$ via the chemisorption reaction (**4**) which has the largest calculated ΔE = −1.69 eV at CCSD(T) in the series.

Optimized Structures

Figure 2 depicts the optimized structures of C_1 $B_{13}(H_2O)^+$ (**1**), C_2 $B_{13}(H_2O)_2^+$ (**2**), C_1 $B_{12}H(H_2O)^+$ (**3**), and C_1 $B_{12}H^+$ (**4**) at PBE0-D3/6-311+G(d,p) which all prove to be true minima of the systems with the smallest calculated vibration frequencies of 67.14, 69.42, 91.30, and 136.59 cm^{-1}, respectively. With the large calculated HOMO-LUMO energy gaps of ΔE_{gap} = 3.32, 3.50, 3.46 eV, and 3.68 eV respectively, these observed species all appear to be chemically stable in thermodynamics at room temperatures. More alternative low-lying isomers with a chemisorbed H_2O ligand are collectively shown in Fig. S2, with the relative energies indicated in eV at CCSD(T). As shown in Fig. 2 and Fig. S2(a), the first H_2O coordinates the B_{13}^+ ($B_3@B_{10}^+$) core at a tricoordinate periphery B atom in the outer B_{10} ring, forming the most stable isomer C_1 $B_{13}(H_2O)^+$ (**1**) which lies 0.09 eV more stable than C_s $B_{13}(H_2O)^+$ (1b). The second H_2O also favors to be chemisorbed molecularly at a tricoordinate periphery B atom in $B_{13}(H_2O)^+$ (**1**) to produce the axially chiral C_2 $B_{13}(H_2O)_2^+$ (**2**) which is found to be 0.15 eV more stable than the second lowest-lying isomer (2b) at CCSD(T) (Fig. S2(b)). The H_2O ligand in C_1 $B_{12}H(H_2O)^+$ (**3**) generated from reaction (**4**) is also chemisorbed to a tricoordinate periphery B atom of the quasi-planar B_{12} core next to the terminal H. Detailed natural atomic charge and electrostatic potential surface analyses in Fig. S3 indicate that the most reactive sites in C_{2v} B_{13}^+ and $C_1B_{12}H(H_2O)^+$ towards H_2O possess the highest natural atomic charges on the B_{10} and B_9 outer rings to produce C_1 $B_{13}(H_2O)^+$ (**1**) and C_1 $B_{12}H(H_2O)^+$ (**3**), respectively, while, as shown in Fig. S2, the second H_2O ligand in the axially chiral C_2 $B_{13}(H_2O)_2^+$ (**2**) is adsorbed onto the second most electron-depleted periphery B atom which appears to be 0.28 eV and 0.38 eV more stable than the sixth isomer C_1 $B_{13}(H_2O)_2^+$ (**2g**) and seventh isomer C_1 $B_{13}(H_2O)_2^+$ (**2i**) at CCSD(T) level, respectively, possibly due to sterical effects. H_2O molecules adsorbed on the surface rather than on the edges of B_{13} and B_{12} cores prove to be obviously less favorable thermodynamically, as shown in Fig. S2 in the cases of **1c**, **2l**, and **4h**.

Extensive BOMD simulations in Fig. S4 indicate that, with the small calculated root mean square deviations of RMSD = 0.05, 0.05 and 0.05 Å and maximum bond length deviations of MAXD = 0.13, 0.15 and 0.12Å, respectively, the experimentally observed boron water complexes $B_{13}(H_2O)^+$ (**1**), $B_{13}(H_2O)_2^+$ (**2**), and $B_{12}H(H_2O)^+$ (**3**) are all dynamically stable at 300 K. No chemical bond breakages, structural distortions, or more stable low-lying isomers were observed during BOMD simulations in 50 ps at room temperature.

Chemisorption Pathways

The optimized chemisorption pathways and potential energy profiles of the experimentally observed $B_{13}(H_2O)^+$ (**1**), $B_{13}(H_2O)_2^+$ (**2**), and $B_{12}H(H_2O)^+$ (**3**) boron water complexes with respect to reactions (**1**), (**2**), and (**4**) are collectively shown in Fig. 3, respectively, with the intermediate and transition-state structures optimized at PBE0 and their

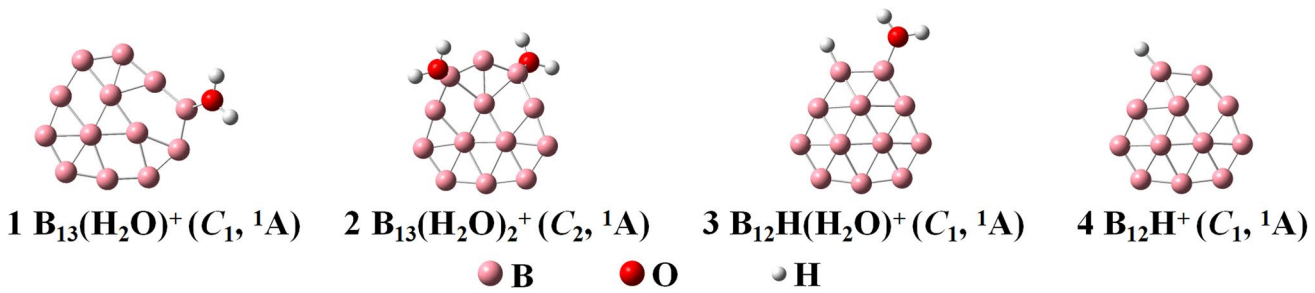

Fig. 2 Optimized structures of the experimentally observed C_1 $B_{13}(H_2O)^+$ (**1**), C_2 $B_{13}(H_2O)_2^+$ (**2**), C_1 $B_{12}H(H_2O)^+$ (**3**), and C_1 $B_{12}H^+$ (**4**) at PBE0-D3/6-311+G(d,p) level

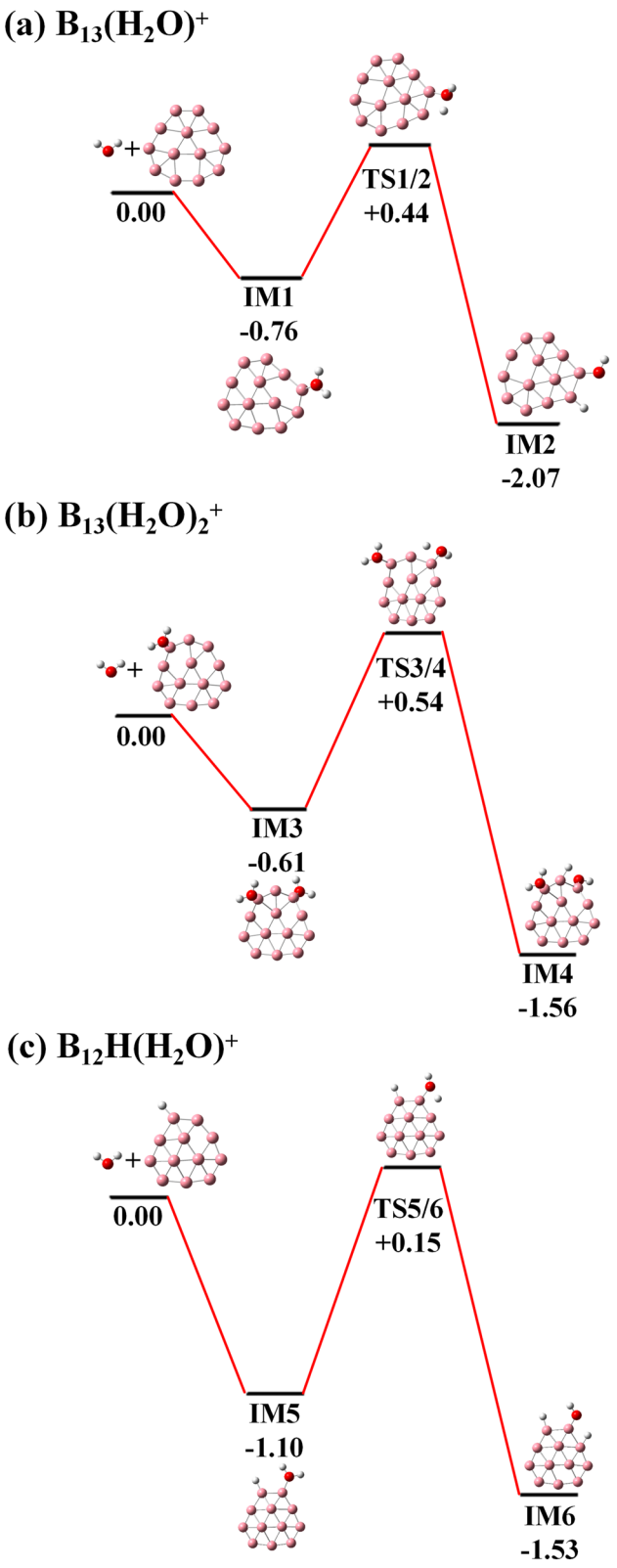

Fig. 3 Optimized chemisorption pathways and potential energy profiles of (**a**) C_1 $B_{13}(H_2O)^+$ (**1**), (**b**) C_2 $B_{13}(H_2O)_2^+$ (**2**), and (**c**) C_1 $B_{12}H(H_2O)^+$ (**3**), with the relative Gibbs free energies indicated in eV at CCSD(T) with the entropy effects considered at 298 K

relative Gibbs free energies indicated at CCSD(T) level with entropy effects considered. As shown in Fig. 3a and Fig. S5(a), the more electronegative O atom in H_2O ligand is chemisorbed onto a tricoordinate periphery B atom in the B_{13}^+ core in a barrierless process, resulting in C_1 $B_{13}(H_2O)^+$ (**1**) with the chemisorption energy of 0.76 eV. However, activation of the H_2O ligand in $B_{13}(H_2O)^+$ (**1**) to form the transition state TS1/2 requires to overcome an energy barrier of +0.44 eV to produce IM2 which contains a H terminal and an OH

group around the B_{13}^+ core (Fig. 3a), indicating that B_{13}^+ cannot activate H_2O under ambient condition to form IM2. The mass peak observed at m/z = 161 in Fig. 1(b) therefore corresponds to the H_2O-chemisorption product of $B_{13}(H_2O)^+$ (**1**). Similarly, $B_{13}(H_2O)_2^+$ (**2**) can also be formed from $B_{13}(H_2O)^+$ (**1**) in a barrier-less process (Fig. S5(b)), while, as shown in Fig. 3(b), activation of the second H_2O ligand in $B_{13}(H_2O)_2^+$ (**2**) with a chemisorption energy of 0.61 eV encounters an energy barrier of +0.54 eV at TS3/4 to form IM4. $B_{13}(H_2O)_2^+$ (**2**) thus represents the mass peak at m/z = 179. As shown in Fig. 3c, activation of the H_2O ligand in $B_{12}H(H_2O)^+$ (**3**) encounters an energy barrier of +0.15 eV at TS5/6 to produce IM6, the mass signal at m/z = 151 should therefore originate from $B_{12}H(H_2O)^+$ (**3**). These results show that the H_2O ligands in $B_{13}(H_2O)^+$ (**1**), $B_{13}(H_2O)_2^+$ (**2**), and $B_{12}H(H_2O)^+$ (**3**) are all molecularly chemisorbed to the quasi-planar B_{13} or B_{12} moieties. No H_2O activations are kinetically favorable in these boron water complexes.

Bonding Pattern Analyses

To better comprehend the high stability of the observed species, detailed AdNDP bonding analyses are performed on $B_{13}(H_2O)^+$ (**1**), $B_{13}(H_2O)_2^+$ (**2**), $B_{12}H(H_2O)^+$ (**3**), and $B_{12}H^+$ (**4**) in Fig. 4. Figure 4a shows that $B_{13}(H_2O)^+$ (**1**) possesses 1 1c-2e lone pair on the O atom in H_2O ligand, 1 2c-2e B-O σ-bond between the H_2O ligand and B_{13}^+ core, 2 2c-2e O-H σ-bonds on H_2O ligand, 10 2c-2e B-B σ-bonds along the B_{10} outer ring in the B_{13}^+ core, 4 3c-2e, 1 4c-2e, and 1 5c-2e σ-bonds on the B_{13}^+ moiety. The remaining six valence electrons are completely delocalized in 3 13c-2e delocalized π-bonds over the B_{13} framework, making $B_{13}(H_2O)^+$ (**1**) π-aromatic in nature analogous to benzene C_6H_6. As shown in Fig. 4b, with one more H_2O ligand introduced in, $B_{13}(H_2O)_2^+$ (**2**) exhibits 2 1c-2e lone pair on two O atoms, 2 2c-2e B-O σ-bonds between the B_{13}^+ core and two H_2O ligands, 4 2c-2e O-H σ-bonds on two H_2O ligands,10 2c-2e B-B σ-bonds along the B_{10} outer ring, 5 3c-2e and 1 4c-2e σ-bonds on the B_{13}^+ core, and 3 13c-2e π-bonds over the slightly wrinkled B_{13}^+ core, again rendering π-aromaticity and extra stability to the system. Similarly, $B_{12}H(H_2O)^+$ (**3**) has 1 1c-2e lone pair on O atom, 2 2c-2e O-H σ-bonds

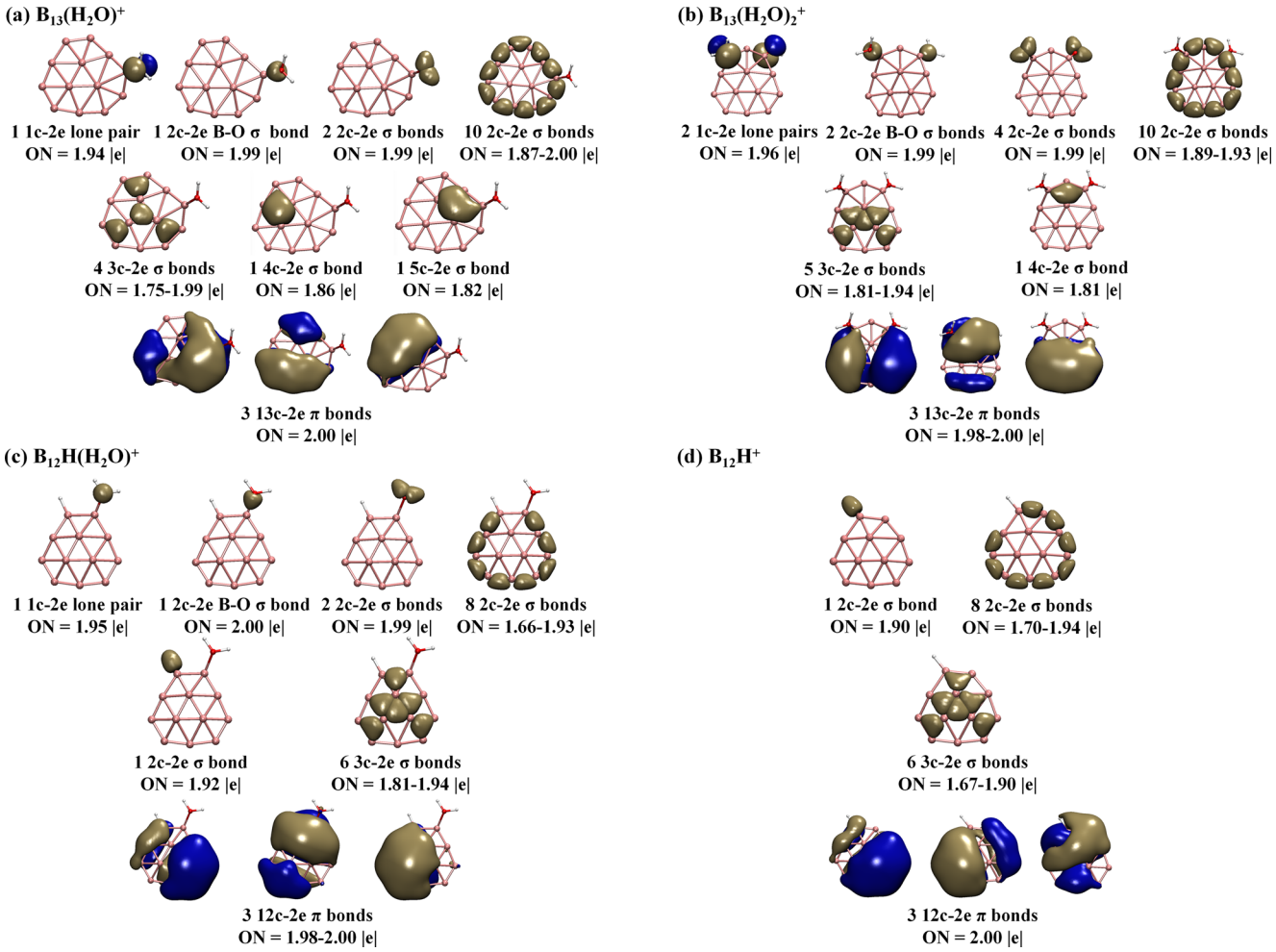

Fig. 4 AdNDP bonding patterns of (**a**) $B_{13}(H_2O)^+$ (**1**), (**b**) $B_{13}(H_2O)_2^+$ (**2**), (**c**) $B_{12}H(H_2O)^+$ (**3**), and (**d**) $B_{12}H^+$ (**4**), with the occupation numbers (ON) indicated

on H_2O ligand, 1 2c-2e B-H σ-bond, 1 2c-2e B-O σ-bond, 8 2c-2e σ-bonds on the B_9 outer ring, 6 3c-2e σ bonds on the B_{12} moiety, and more interestingly, 3 12c-2e π-bonds totally delocalized over the slightly buckled B_{12} core (Fig. 4c), making the monocation π-aromatic in nature analogous to benzene. Similar to $B_{12}H(H_2O)^+$ (**3**), the experimentally observed $B_{12}H^+$ (**4**) in Fig. 1b also appears to possess 3 12c-2e delocalized π-bonds over the B_{12} moiety (Fig. 4d). Thus, all the four species $B_{13}(H_2O)^+$ (**1**), $B_{13}(H_2O)_2^+$ (**2**), $B_{12}H(H_2O)^+$ (**3**), and $B_{12}H^+$ (**4**) observed in experiments are π-aromatic in nature analogous to benzene C_6H_6.

Boron Bonds Analyses

Detailed EDA-NOCV analyses in Fig. 5 and Table S1 reveal the coordination bonding patterns in these complexes more specifically, with the corresponding deformation densities Δρ and shapes of the most important interacting orbitals of the pairwise orbital interactions extracted in Fig. 5. As shown in Fig. 5(a), the effective σ-donation from the HOMO-1 of H_2O to LUMO of B_{13}^+ occupies 70.56% of the overall orbital interaction between B_{13}^+ and H_2O in $B_{13}(H_2O)^+$ (**1**). The weak π-donation from the HOMO of H_2O to LUMO+3 of B_{13}^+, σ-donation from the HOMO-1 of H_2O to LUMO+5 of B_{13}^+, and π-back-donation from HOMO-5 of B_{13}^+ to LUMO+3 of H_2O contribute 13.56%, 10.34%, and 5.58% to the overall interaction, respectively. Similar in-phase orbital interactions exist in $B_{13}(H_2O)_2^+$ (**2**) (Fig. 5(b)) and $B_{12}H(H_2O)^+$(**3**) (Fig. 5(c)), with the dominant σ-donations from the HOMO-1 of H_2O to LUMO of $B_{13}(H_2O)^+$ and from the HOMO-1 of H_2O to LUMO of $B_{12}H^+$ contribute 73.88% in $B_{13}(H_2O)_2^+$ (**2**) and 70.80% in $B_{12}H(H_2O)^+$(**3**), respectively. These σ-donation interactions are well reflected in the AdNDP 2c-2e B-O σ-bonds in Fig. 4 which mainly originate from the in-phase LP(H_2O:)→LV(B) orbital overlaps between the electronegative O atom in H_2O as lone-pair (LP) σ-donor and periphery electron-deficient B atoms in B_{13}^+ ($B_3@B_{10}^+$) and $B_{12}H^+$ ($B_3@B_9H^+$) with

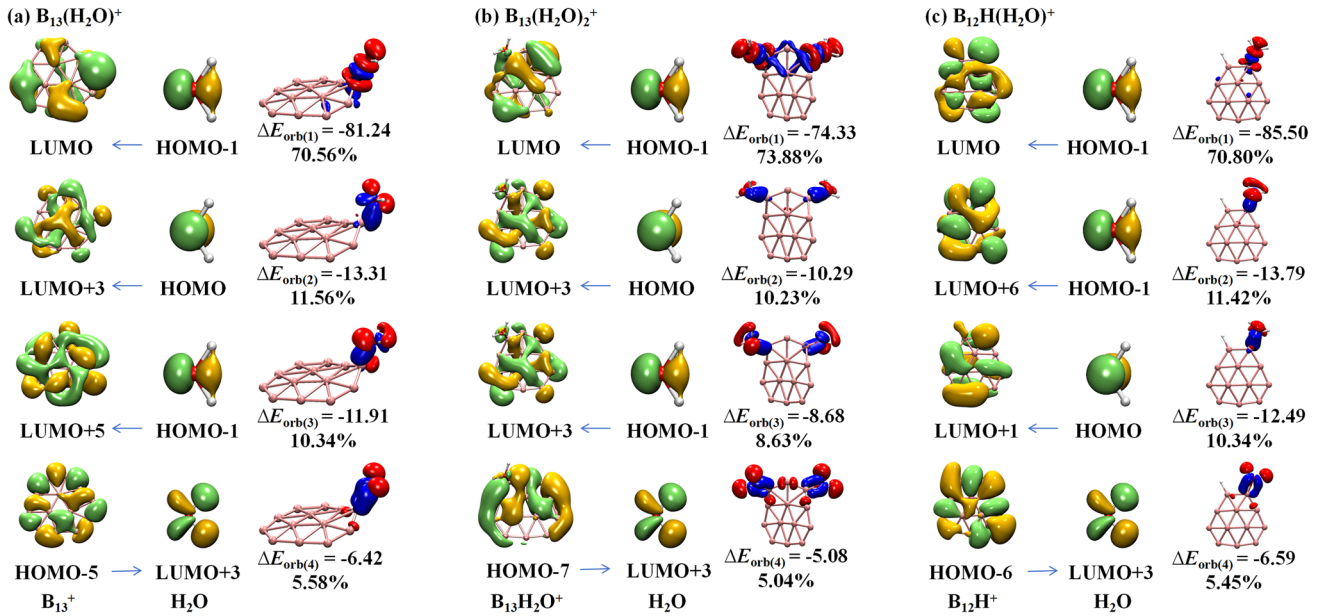

Fig. 5 Plots of the deformation densities Δρ and shapes of the interacting orbitals of the pairwise orbital interactions between (**a**) B_{13}^+ and H_2O in C_1 $B_{13}(H_2O)^+$ (**1**), (**b**) $B_{13}(H_2O)^+$ and H_2O in C_2 $B_{13}(H_2O)_2^+$ (**2**), and (**c**) $B_{12}H^+$ and H_2O in C_1 $B_{12}H(H_2O)^+$ (**3**), with the orbital interaction energies ΔE_{orb} in kcal·mol^{-1} and their percentage contributions to the overall orbital interactions indicated. The color code of the charge flow is from red to blue

lone vacant (LV) orbitals as LP σ-acceptors. As shown in Fig. 5(b) and Fig. 5(c), weak π-donation, σ-donation, and π-back-donation also exist in both $B_{13}(H_2O)_2^+$ (**2**) and $B_{12}H(H_2O)^+$(**3**). With the bond dissociation energies of 1.34, 1.29, 1.69 eV in $B_{13}(H_2O)^+$ (**1**), $B_{13}(H_2O)_2^+$ (**2**), and $B_{12}H(H_2O)^+$ (**3**) at CCSD(T), respectively, the LP(H_2O:)-LV(B) interactions in these boron water complexes occupy only 16.0%, 15.4%, and 20.2% of the bond dissociation energy (8.35 eV) of a typical O–B covalent bond, indicating the existence of the newly proposed boron bonds [19] in these experimentally observed boron water complexes.

The NCI-RDG approach which enables the weak interactions to be graphically visualized has been widely used to identify the types of weak interactions in concerned systems. Johnson et al. developed the reduced density gradient (RDG) approach and defined RDG(r) in the following equation [44]:

$$RDG(r) = \frac{1|\nabla\rho(r)|}{2(3\pi^2)^{\frac{1}{3}}\rho(r)^{\frac{4}{3}}}$$

Figure 6 shows the detailed RDG~sin(λ_2)ρ plots and color-filled RDG isosurfaces of C_1 $B_{13}(H_2O)^+$ (**1**), C_2 $B_{13}(H_2O)_2^+$ (**2**), and $B_{12}H(H_2O)^+$ (**3**). The blue spike 1 around sin(λ_2)ρ ≈ −0.122 a.u. for $B_{13}(H_2O)^+$ (**1**) in Fig. 6(a) corresponds to the color-filled blue RDG isosurface 1 between H_2O and B_{13}^+ in Fig. 6(a'), indicating the existence of the LP(H_2O:)→LV(B) boron bond between the O atom in H_2O and a tricoordinate B atom in B_{13}^+ core, while C_2 $B_{13}(H_2O)_2^+$ (**2**) exhibits an even better separated blue spike 1 with a small negative sign(λ_2)ρ = −0.105 a.u. in Fig. 6(b) which corresponds to the color-filled blue isosurfaces between the two equivalent H_2O ligands and B_{13}^+ core in Fig. 6(b′), again confirming the existence of LP(H_2O:)→LV(B) boron bond in the complex system. The blue spike with a slightly more negative sign(λ_2)ρ = −0.125 a.u. in $B_{12}H(H_2O)^+$ (**3**) also corresponds to the isosurface between $B_{12}H^+$ and H_2O in Fig. 6(c'). The blue spikes between sin(λ_2)ρ = −0.105 ~ −0.125 a.u. in Fig. 5 thus well support the existence of LP(H_2O:)→LV(B) boron bonds in these experimentally observed boron water complexes. These LP(H_2O:)→LV(B) boron bonds which possess about 15 ~ 20% of the dissociation energy of a typical O–B covalent bond appear to be much stronger than both typical hydrogen bonds (HBs) and halogen bonds (XBs), with the latter possessing obviously smaller negative sin(λ_2)ρ values [48, 49] than the former.

Conclusion

Combined experimental and theoretical investigations performed in this work show that the perfect planar C_{2v} B_{13}^+ can react with H_2O in gas phase to form a series of quasi-planar aromatic boron water complexes C_1 $B_{13}(H_2O)^+$ (**1**), C_2 $B_{13}(H_2O)_2^+$ (**2**), and C_1 $B_{12}H(H_2O)^+$ (**3**) analogous to benzene, evidencing the existence of LP(H_2O:)→LV(B) boron bonds in chemistry which occupy about 15 ~ 20% of the dissociation energy of a typical O–B covalent bond.

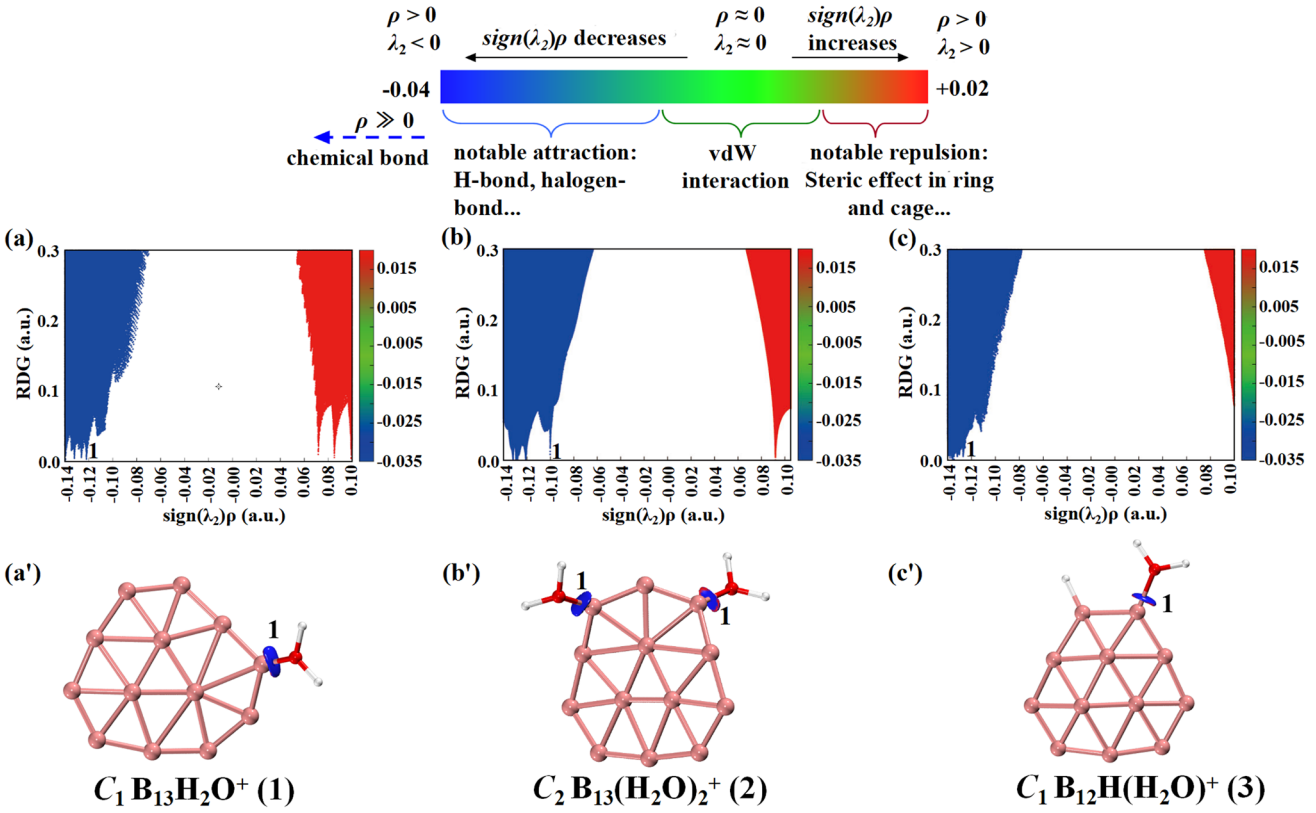

Fig. 6 Calculated RDG ~ sign(λ_2)ρ plots ((**a**), (**b**), and (**c**)) and color-filled RDG isosurfaces ((**a′**), (**b′**), and (**c′**)) of $B_{13}(H_2O)^+$ (**1**), $B_{13}(H_2O)_2^+$ (**2**), and $B_{12}H(H_2O)^+$ (**3**)

These findings provide important insights to design and produce novel boron water (H_2O), boron carbonyl (CO), and boron ammonia (NH_3) complexes which are expected to be effectively stabilized by boron bands. Joint experiment and theory investigations on LP(H_3N:)→LV(B) boron bands in boron ammonia complexes $B_m(NH_3)_n^{+/0/-}$ are currently in progress.

Supplementary Information The online version contains supplementary material available at https://doi.org/10.1007/s10876-025-02897-w.

Authors' Contributions S-D Li and Q Chen designed the project and T Zhang, R-N Yuan performed the experiments and calculations. All the authors participate in the discussion and preparation of the manuscript.

Funding The work was supported by the National Natural Science Foundation of China (22373061 and 92461303 to S.-D. Li and 22003034 to Q. Chen).

Data Availability No datasets were generated or analysed during the current study.

Declarations

Competing interests The authors declare no competing interests.

References

1. A. N. Alexandrova, A. I. Boldyrev, H. J. Zhai, and L. S. Wang (2006). *Chem. Rev.* **250**, 2811–2866.
2. L. S. Wang (2016). *Int. Phys. Chem.* **35**, 69142.
3. T. Jian, X. Chen, S. D. Li, A. I. Boldyrev, and L. S. Wang (2019). *Chem. Soc. Rev.* **48**, 3550–3591.
4. H. Bai, T. T. Chen, Q. Chen, X. Y. Zhao, Y. Y. Zhang, W. J. Chen, W. L. Li, L. F. Cheung, B. Bai, J. Cavanagh, W. Huang, S. D. Li, J. Li, and L. S. Wang (2019). *Nanoscale.* **11**, 23286–23295.
5. H. J. Zhai, Y. F. Zhao, W. L. Li, Q. Chen, H. Bai, H. S. Hu, Z. A. Piazza, W. J. Tian, H. G. Lu, Y. B. Wu, et al. (2014). *Nat. Chem.* **6**, 727–731.
6. Q. Chen, W. L. Li, Y. F. Zhao, S. Y. Zhang, H. S. Hu, H. Bai, H. R. Li, W. J. Tian, H. G. Lu, H. J. Zhai, S. D. Li, J. Li, and L. S. Wang (2015). *ACS Nano.* **9**, 754–760.
7. W. J. Chen, Y. Y. Ma, T. T. Chen, M. Z. Ao, D. F. Yuan, Q. Chen, X. X. Tian, Y. W. Mu, S. D. Li, and L. S. Wang (2021). *Nanoscale.* **13**, 3868–3876.
8. E. Oger, N. R. Crawford, R. Kelting, P. Weis, M. M. Kappes, and R. Ahlrichs (2007). *Angew. Chem. Int. Ed.* **46**, 8503–8506.
9. L. Hanley, J. L. Whitten, and S. L. Anderson (1988). *J. Chem. Phys.* **92**, 5803–5812.
10. A. Ricca and C. W. Bauschlicher Jr. (1996). *Chem. Phys.* **208**, 233–242.
11. Y. G. Yang, D. M. Jia, Y. J. Wang, H. J. Zhai, Y. Man, and S. D. Li (2017). *Nanoscale.* **9**, 1443–1448.
12. J. Zhang, A. P. Sergeeva, M. Sparta, and A. N. Alexandrova (2012). *Angew. Chem. Int. Ed.* **51**, 8512–8515.

13. R. N. Yuan, J. J. Chen, Q. Chen, Q. W. Zhang, H. Niu, R. Wei, Z. H. Wei, X. N. Li, and S. D. Li (2024). *J. Am. Chem. Soc.* **146**, 31464–31471.
14. R. N. Yuan, Q. Chen, H. Niu, C. Y. Gao, X. N. Zhao, Y. B. Wu, S. G. He, and S. D. Li (2025). *Phys. Chem. Chem. Phys.* **27**, 7279–7289.
15. P. A. Hintz, S. A. Ruatta, and S. L. Anderson (1990). *J. Chem. Phys.* **92**, 292–303.
16. X. Y. Sun, J. G. Du, L. Zhao, and G. Jiang (2020). *J. Mol. Liq.* **315**,113759.
17. Y. Valadbeigi, H. Farrokhpour, and M. Tabrizchi (2015). *J. Chem. Sci.* **127**, 2029–2038.
18. K. Kurotobi and Y. Murata (2011). *Science.* **333**, 613–616.
19. T. Zhang, C. Y. Gao, X. N. Zhao, G. Y. Han, and S. D. Li (2025). *J Mol Model*. https://doi.org/10.1007/s00894-024-06276-6.
20. X. N. Wu, B. Xu, J. H. Meng, and S. G. He (2012). *Int. J. Mass Spectrom.* **310**, 57–64.
21. Z. Yuan, Y. X. Zhao, X. N. Li, and S. G. He (2013). *Int. J. Mass Spectrom.* **354–355**, 105–112.
22. R. A. J. O'Hair (2006). *Chem. Commun.* **14**, 1469–1481.
23. L. D. Socaciu, J. Hagen, U. Heiz, T. M. Bernhardt, T. Leisner, and L. Wöste (2001). *Chem. Phys. Lett.* **340**, 282–288.
24. C. Adamo and V. Barone (1999). *J. Chem. Phys.* **110**, 6158–6170.
25. R. Krishnan, J. S. Binkley, R. Seeger, and J. A. Pople (1980). *J. Chem. Phys.* **72**, 650–654.
26. S. Grimme, J. Antony, S. Ehrlich, and H. Krieg (2010). *J. Chem. Phys.* **132**,154104.
27. M. J. Frisch, G. W. Trucks, H. B. Schlegel, G. E. Scuseria, M. A. Robb, J. R. Cheeseman, et al (2016) Gaussian 16, revision A.03, Gaussian Inc, Wallingford CT.
28. G. D. Purvis and R. J. Bartlett (1982). *J. Chem. Phys.* **76**, 1910–1918.
29. G. E. Scuseria and H. F. Schaefer (1989). *J. Chem. Phys.* **90**, 3700–3703.
30. T. J. Lee and P. R. Taylor (2009). *Int. J. Quantum. Chem.* **36**, 199–207.
31. J. V. Vondele, M. Krack, F. Mohamed, M. Parrinello, T. S. Chassaing, and J. Hutter (2005). *Commun.* **167**, 103–128.
32. S. Goedecker, M. Teter, and J. Hutter (1996). *Phys. Rev. B.* **54**, 1703–1710.
33. W. L. Li, K. X. Chen, E. Rossomme, M. Head-Gordon, and T. Head-Gordon (2021). *J. Phys. Chem. Lett.* **12**, 10304–10309.
34. C. Gonzalez and H. B. Schlegel (1989). *J. Chem. Phys.* **90**, 2154–2161.
35. C. Gonzalez and H. B. Schlegel (1990). *J. Phys. Chem.* **94**, 5523–5527.
36. N. V. Tkachenko and A. I. Boldyrev (2019). *Phys. Chem. Chem. Phys.* **21**, 9590–9596.
37. T. Ziegler and A. Rauk (1977). *Theor. Chim. Acta.* **46**, 1–10.
38. M. P. Mitoraj, A. Michalak, and T. Ziegler (2009). *J. Chem. Theory. Comput.* **5**, 962–975.
39. M. Mitoraj and A. Michalak (2007). *Organometallics.* **26**, 6576–6580.
40. G. Te Velde, F. M. Bickelhaupt, E. J. Baerends, C. Fonseca Guerra, S. J. A. Van Gisbergen, J. G. Snijders , T. Ziegler (2001). *J. Comput. Chem.* **22**, 931-967.
41. J. L. Heully, I. Lindroth, E. Lindroth, S. Lundqvist, and A. M. Martensson-Pendrill (1986). *J. Phys. B: At. Mol. Phys.* **19**, 2799–2815.
42. C. Chang, M. Pelissier, and P. Durand (1986). *Phys. Scr.* **34**, 394–404.
43. E. Van Lenthe, R. Van Leeuwen, E. J. Baerends, and J. G. Snijders (1996). *J. Chem. Phys.* **57**, 281–293.
44. E. R. Johnson, S. Keinan, P. Mori-Sánchez, J. Contreras-García, A. J. Cohen, and W. Yang (2010). *J. Am. Chem. Soc.* **132**, 6498–6506.
45. G. Saleh, C. Gatti, and L. L. Presti (2012). *Comput. Theor. Chem.* **998**, 148–163.
46. T. Lu and F. Chen (2012). *J. Comput. Chem.* **33**, 580–592.
47. W. Humphrey, A. Dalke, and K. Schulten (1996). *J. Mol. Grap.* **14**, 33–38.
48. C. Y. Gao , Y. Y. Ma, Q. Chen, and S. D. Li (2024). J. Clust. Sci. 35, 693-700.
49. C. Y. Gao, B. B. Pei, and S. D. Li (2025). *J. Comput. Chem*. **46**, e2783